Geophysical Research Letters

RESEARCH LETTER
10.1029/2023GL104243

Key Points:

- A semi-empirical model for turbulent Alfvénic fields in the storm-time inner-magnetosphere is created
- Alfvénic turbulence drives rapid radiation belt electron transport across *L*-shells, through pitch-angles and in momentum space
- The combined action of the EM field vector components increases transport rates - this transport is not necessarily classically diffusive

Supporting Information:

Supporting Information may be found in the online version of this article.

Correspondence to:
C. C. Chaston,
ccc@ssl.berkeley.edu

Citation:
Chaston, C. C. (2023). Electron scattering, transport and energization by Alfvénic turbulence in Earth's outer radiation belt. *Geophysical Research Letters*, *50*, e2023GL104243. https://doi.org/10.1029/2023GL104243

Received 21 APR 2023
Accepted 14 JUN 2023

Electron Scattering, Transport and Energization by Alfvénic Turbulence in Earth's Outer Radiation Belt

C. C. Chaston[1]

[1]Space Sciences Laboratory, University of California, Berkeley, Berkeley, CA, USA

Abstract The transport of energetic electrons immersed in Alfvénic turbulence in Earth's outer radiation belt is explored. It is shown how electrons subject to the action of an empirically derived 3-D spectrum of Alfvénic field fluctuations experience rapid transport across *L*-shells, pitch-angle and through momentum space. Timescales for radial transport are less than a drift period while scattering at large pitch-angle occurs at a similar rate. Transport through momentum space occurs at a rate comparable to that in whistler mode chorus and is particularly rapid below 100 keV. Bounce-averaged transport coefficients for these processes are consistent with quasi-linear estimates for drift-bounce resonances, albeit with enhanced values. A super-diffusive to sub-diffusive transition with increasing energy is identified.

Plain Language Summary Space weather events known as geomagnetic storms drive rapid variations in near-Earth energetic particle distributions with potentially catastrophic effect. Populations of energetic electrons trapped for months in Earth's outer radiation belt during these storms are sometimes lost in a matter of hours. While large-scale deformation of the geomagnetic field due to the impact of explosive solar energy releases is an obvious driver of this variability, turbulent storm-time electromagnetic fluctuations known as Alfvén waves on the scale of energetic electron orbits may also drive rapid changes. Motivated by coincident observations of this turbulence and rapid variations in Earth's outer radiation belt, a numerical experiment is performed to evaluate the effectiveness of these fluctuations in modifying radiation belt electron populations. Using the statistical properties of the observed wavefields and of the supporting plasma, a wave model equivalent to that observed is created. Energetic electrons within this model experience erratic deviations from their usual orbits. Statistical analyses quantifying these deviations indicate anomalous transport rates through space on timescales of the order of minutes along with rapid variations in particle momentum and energy. The results from this numerical experiment suggest that turbulent electromagnetic fields may play an important role in storm-time radiation belt dynamics.

1. Introduction

The variability of the Earth's outer radiation belt during geomagnetic storms requires processes that act on timescales that are short relative to storm-phase (Baker et al., 2016; Mauk et al., 2012). Deformation of Earth's geomagnetic field in response to impulsive solar wind pressure variations and associated changes in the interplanetary magnetic field is perhaps the leading cause of broad-range storm time "drop-outs" of radiation belt populations (Turner et al., 2012). However, this is not the only process active in the modulation of radiation belt electron fluxes during these times (Horne and Thorne, 1998; Millan & Thorne, 2007; Ozeke et al., 2017). Furthermore, the transverse scales of pervasive storm-time broad-band electromagnetic fluctuations outside the plasmapause in the ULF/ELF range coincide with the gyro-radii of radiation belt electrons (Chaston et al., 2015). These fluctuations may act to violate the invariants governing electron motion through the inner magnetosphere and drive rapid transport across *L*-shells and scattering through pitch-angle (Chaston, Bonnell, Wygant, et al., 2018; Chaston, Bonnell, Halford, et al., 2018; Chaston et al., 2017; Shen et al., 2022a; Shen et al., 2022b).

A characteristic of the broad-spectrum field variations distinct from observations of the classical ULF wave spectrum, is their mixed polarization and deviation from planarity (Chaston et al., 2020). These characteristics, combined with a distinctive power-law spectrum as a function of spacecraft frame frequency (f_{sc}) are more characteristic of electromagnetic turbulence than MHD resonances of the geomagnetic field often used to account for the inner magnetospheric ULF spectrum (Rae et al., 2019). Nonetheless, cross-spectral analyses of orthogonal electric and magnetic fields comprising the broad-band spectrum reveal phase relationships consistent with the presence of field-line eigenmodes and counter-propagation. These modes appear as a continuum over a range of f_{sc} where the wave impedance matches that of dispersive Alfvén waves with phase speeds less than the local plasma convection (Chaston et al., 2015). Consequently, f_{sc} is largely defined by the Doppler shift of advected structure analogous to turbulent cascades of Alfvén waves in the solar wind (Bale et al., 2005) but constrained by the closed field geometry of the inner magnetosphere (Chaston, 2022; Chaston et al., 2014).

Observations have shown that field variations of this kind should be important for energetic electron dynamics in Earth's outer radiation belt and inner plasma sheet. Measurements from balloons (Chaston, Bonnell, Halford, et al., 2018) and cube-sats (Shen et al., 2022b) magnetically conjugate with satellites during wave events provide evidence that such waves drive radiation belt electron loss, while energized distributions in similar fluctuations provide a radiation belt source population (Usanova and Ergun, 2022). To explore these processes the trajectories of energetic electrons on closed field-lines immersed in an empirically derived 3-dimensional spectrum of fluid-kinetic fluctuations in the outer radiation belt are examined and used to derive transport coefficients through space (L-shell), pitch-angle (θ) and momentum (p). This approach makes no assumption that such transport is diffusive in nature, nor does it a priori prescribe a mechanism through which this transport occurs.

2. Wave Model

A model for broad-band Alfvénic fluctuations along geomagnetic field-lines between ionospheres is provided via a two-fluid/fluid kinetic approach, formulated in terms of the scalar (Φ) and field-aligned vector potentials (A_μ) in dipole coordinates (ν,ϕ,μ) (Chaston et al., 2016). Here, ν points radially outward from a given L-shell, ϕ is the azimuthal coordinate and μ is geomagnetic field-aligned. A_μ is assumed periodic as a function of L and ϕ with form,

$$A_\mu = A_\mu(\mu) e^{i\left(\frac{2\pi\nu}{\alpha} + m\phi - \omega t + \delta\right)} \tag{1}$$

where α is the fraction of an L-shell corresponding to one wavelength in ν, m is the azimuthal wavenumber, ω is the wave frequency and δ a phase shift. Periodicity in the transverse plane provides differential operators for wavelengths in ν and ϕ small relative to plasma gradient scales that can be approximated in terms of local wave vectors with $k_\nu \approx 2\pi/(h_\nu\alpha)$, $k_\phi \approx m/h_\phi$ and $k_\perp^2 = k_\nu^2 + k_\phi^2$. Here h_ν, h_ϕ and h_μ are the metrics for the dipole coordinate system (Cummings et al., 1969). The wave equation is then,

$$\omega^2 \lambda_e^2 \nabla^2 A_\mu + \nabla_\mu \frac{\upsilon_A^2 \chi}{|\nabla^2|} \left(\frac{4\pi^2}{\alpha^2} \frac{1}{h_\nu h_\phi} \nabla_\mu \frac{h_\phi}{h_\nu} A_\mu + \frac{m^2}{h_\nu h_\phi} \nabla_\mu \frac{h_\nu}{h_\phi} A_\mu \right) + \frac{\rho_s^2 \upsilon_A^2}{T_e} \nabla_\mu \frac{T_e}{h_\nu h_\phi} \nabla_\mu h_\nu h_\phi \nabla^2 A_\mu + \omega^2 A_\mu = 0 \tag{2}$$

where λ_e is the electron inertial length, $\nabla^2 \approx k_\perp^2$, $\nabla_\mu = \frac{1}{h_\mu}\frac{\partial}{\partial\mu}$, ρ_s is the ion acoustic gyro-radius, $\chi \approx k_\perp^2 \rho_i^2 / \left[1 - I_o\left(k_\perp^2 \rho_i^2\right) e^{-k_\perp^2 \rho_i^2}\right]$ is a finite gyro-radii correction (Johnson and Cheng, 1997) with I_o the zeroth order modified Bessel function. The electromagnetic fields are then given by solving the wave equation for A_μ with $\boldsymbol{b}_\perp = \nabla \times A_\mu$, $E = -\nabla\Phi - \partial A_\mu/\partial t$ and,

$$\boldsymbol{\Phi} \approx -i \frac{\upsilon_A^2 \chi}{\omega k_\perp^2} \left[\frac{k_\nu}{h_\phi h_\mu} \frac{\partial(h_\phi k_\nu A_\mu)}{\partial\mu} + \frac{k_\phi}{h_\nu h_\phi} \frac{\partial(h_\nu k_\phi A_\mu)}{\partial\mu} \right] \tag{3}$$

The derivation of Equations 2 and 3 is provided in Chaston et al. (2016). For simplicity in solving Equation 2 an infinitely conducting ionosphere is assumed where $\boldsymbol{\Phi} = 0$ and eigenmode solutions derived iteratively via a "shooting" method for the semi-empirical plasma profiles detailed in Supporting Information S1.

To examine the trajectories of radiation belt electrons in the observed broad-band fluctuations the observed spectrum is replicated by superimposing 100 eigenmodes centered on $L = 5.7$ spaced logarithmically in wavenumber over the range with $0.1 \le k_\perp \rho_{ieq} \le 10$ where the "eq" subscript indicates values at the equator. This specific L value is selected because it is central to the range of L-shells over which these fluctuations are observed and is where published measurements of the field structure have been reported. These modes comprise a range of field-line harmonics with fixed amplitude over the duration of the simulation and increasing obliquity with increasing $k_\perp$. Filamentary structure is generated by pairing the eigenmodes at each $k_\perp$ as,

$$k_{1Leq} = k_\perp \cos\theta_w, k_{1\phi eq} = k_\perp \sin\theta_w$$

$$k_{2Leq} = k_{\perp} \cos(\theta_w + \theta_f), k_{2\phi eq} = k_{\perp} \sin(\theta_w + \theta_f) \tag{4}$$

where θ_w and $\theta_w + \theta_f$ are the angles between the radial direction and $\boldsymbol{k}_{1\perp eq}$ and $\boldsymbol{k}_{2\perp eq}$ respectively. The eigenmodes comprising each pair together define an array of time varying elliptical loops of magnetic field with eccentricity, or filamentation, $\mathcal{F} = tan(\theta_f/2)$ ranging between zero (planar current sheets) and one (cylindrical current filaments). θ_w is randomly distributed between 0 and 2π with $\mathcal{F}$ prescribed to reproduce the observed log-normal distribution in filamentation defined as,

$$\mathcal{F} = e^{\vartheta\eta + \xi} \leq 1 \tag{5}$$

here ϑ is a normally distributed random number with standard deviation 1, and $\eta = 0.51$ and $\xi = -1.21$ are the standard deviation and peak of the distribution in log-space derived from the case study measurements of Chaston et al. (2020).

The amplitude of each eigenmode pair is defined by the statistical spectrum compiled from measurements near the magnetic equator outside the plasmapause (Chaston et al., 2015). This spectrum over the range $0.1 \leq k_{\perp}\rho_{ieq} \leq 10$ varies as $k^{-\zeta}$ with ζ transitioning from 2 to 3. Using this result the amplitude of each mode is given by,

$$b_{\perp}(s) = \sqrt{\varepsilon_{S=1} s^{\zeta} ds} \tag{6}$$

where $s = k_{\perp}\rho_i$, ε_S is in units T^2/ds and $b_{\perp} = \sqrt{b_{\nu}{}^2 + b_{\phi}{}^2}$. The amplitude along the field-line is then defined using $b_{\perp}(s)$ to scale the envelope of the corresponding eigenmode solution with $\zeta = 2$ and $\varepsilon_{s=1} = 4 \times 10^{-18} T^2$ at the equator. δ is randomly distributed over 0 to 2π. While the variation of the solutions across L-shells is described by Equation 1, a finite wave region is imposed by applying a Gaussian in L-shell centered on $L = 5.7$ with width 1. This is representative of the evanescence of the fluctuations with displacement from the L-shell on which the eigenmode solutions are centered (Mann et al., 1995). Note that this profile has negligible effect on the transport results because the particle orbits remain within one standard deviation of the peak while the associated compressional magnetic field can be ignored relative to the wave field amplitudes. The amplitude of each mode in the azimuthal direction is invariant over the range in ϕ through which the particles drift. This is generally less than 45° and less than the longitudinal width of observed wave regions that can extend over several hours of magnetic local time (Hull et al., 2020).

Figures 1a and 1b show a 3-D representation of the wave model in $b_{\perp} = \sqrt{b_{\nu}{}^2 + b_{\phi}{}^2}$ and $E_{\perp} = \sqrt{E_{\nu}{}^2 + E_{\phi}{}^2}$. To allow the equatorial fields to be visible, the color scale is saturated close to the ionosphere providing the inequalities in the upper z-axis labels. Fourier analysis along the synthetic spacecraft trajectory shown through the volume provides the spectra of Figures 1c–1e. The frequency in the "spacecraft" frame is for a relative speed between the plasma and the spacecraft of 30 km/s. This speed returns $s = 1$ at $f_{sc} \approx 0.2$Hz as inferred from statistical wave dispersion/impedance measurements (Chaston et al., 2015) and consistent with $E \times B_0$ drifts during wave events of this kind (Chaston, 2022). Noting that the specific form of the wave spectra is dependent on the trajectory, the spectral scaling of energy density (Figures 1c and 1d) and the associated wave impedance (Figure 1e) qualitatively replicate those reported in the statistics of Chaston et al. (2015). The corresponding filamentation in field-aligned current and flow vorticity is shown in Figures 1f and 1g - these qualitatively reproduce those reported in Chaston et al. (2020). Except for a consideration of intermittency, this model is statistically equivalent to that observed. A movie showing the temporal variation of b_{ν} in the X–Z plane is provided in Supporting Information S1.

3. Particle Simulations

To explore how the wavefields modify the outer radiation belt, electron trajectories over an energy range from 50 keV to 5 MeV are traced after equatorial injection at $L = 5.7$. This is achieved via the solution of the equations of motion defined as,

$$\frac{d\boldsymbol{p}}{dt} = q_e(\boldsymbol{E} + \boldsymbol{v} \times \boldsymbol{B}) \text{ and } \frac{d\boldsymbol{x}}{dt} = \boldsymbol{v} \tag{7}$$

where $\boldsymbol{p} = \gamma m_e \boldsymbol{v}$, γ is the Lorentz factor, m_e is the electron rest mass, $\boldsymbol{v}$ is the electron velocity and $\boldsymbol{x}$ is the particle position. Gravitation has been included in the calculations but makes almost no difference for the energy range considered. The solution is performed using a modified midpoint technique (Press et al., 2002) with a recursive

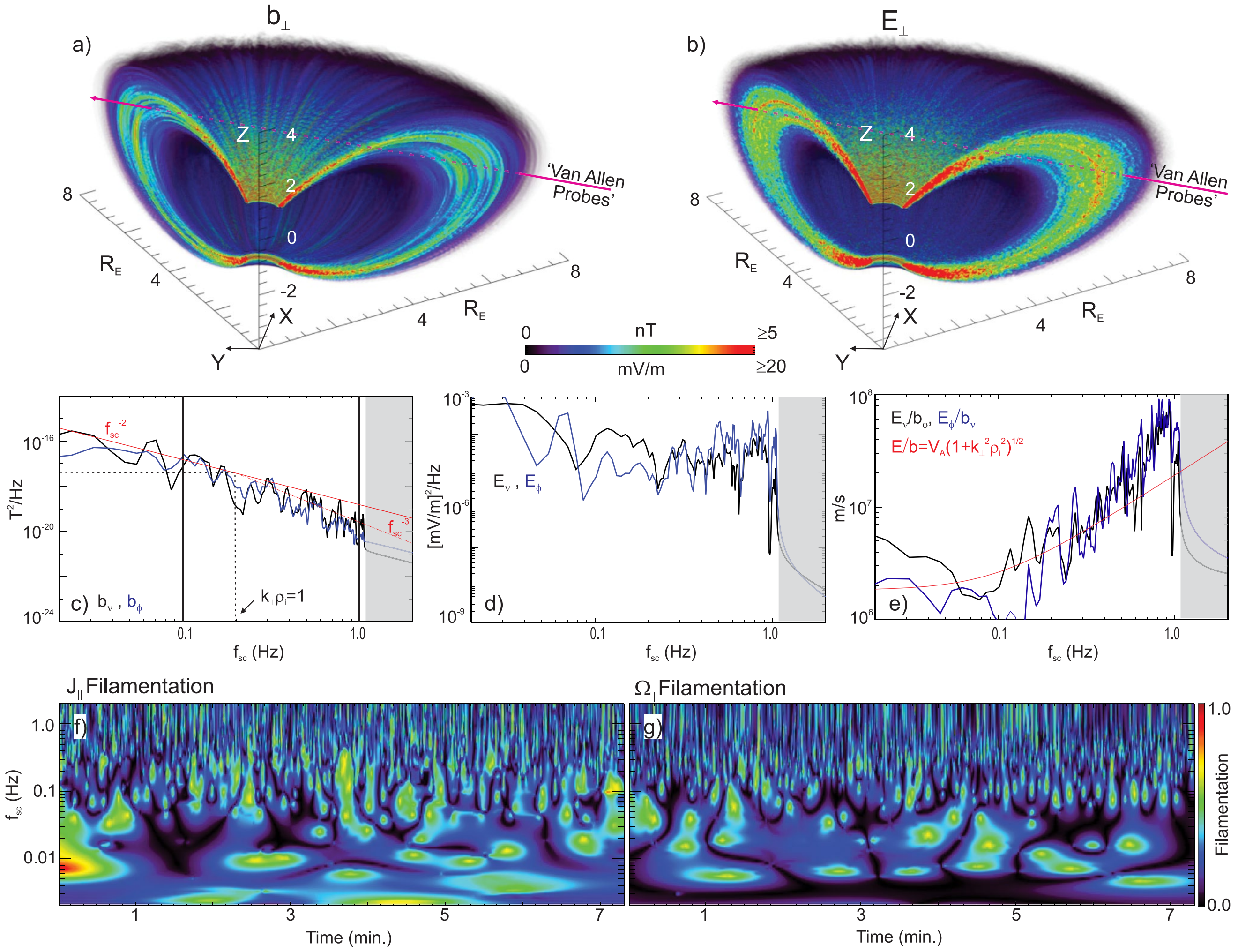

Figure 1. Semi-empirical wave model. (a) and (b) 3-D snapshots of total perpendicular electric and magnetic fields at $t = 0$. (c–e) "Observed" spectral quantities along a Van Allen Probes pass. (f) and (g) Filamentation in field-aligned current, $J_\parallel$, and vorticity, $\Omega_\parallel$, derived from a polarization analysis of $\boldsymbol{b}_\perp$ and $\boldsymbol{E} \times \boldsymbol{B}_0$ velocity fields.

test for convergence at each time step. Alternate solution techniques have been implemented for a limited number of cases to confirm reliability.

Figures 2a and 2b show the trajectory of an $E_n = 500$ keV electron with initial equatorial pitch-angle of $\theta_{eq} = 45°$ over an interval of 45 s. The color gradient along the trajectory represents time, starting with purple-blue shades, then green-yellow, and ending in red while the green-red shading represents a snapshot of b_ν taken midflight. The superposition of the bounce motion between hemispheres over multiple bounces, and motion across L-shells, forms the bright crescent shaped feature in the $\sqrt{X^2 + Y^2}, Z$ plane shown in Figure 2a. With each bounce the latitude of mirroring varies erratically but generally increases with increasing L. Figure 2b shows the trajectory mapped adiabatically into the equatorial plane with the curve thickness representing the projected gyro-diameter. The white curve in the same panel shows the guiding center drift without the wavefields. The fine scale semi-periodic oscillations of the colored curve are a consequence of the displacement of the guiding center due to the action of the wavefields over each bounce between hemispheres. The concatenation of these small displacements as the particle drifts azimuthally leads to the larger scale meandering motion of the guiding center across L-shells corresponding to radial transport.

The erratic variation in L-shell and of the location of mirroring with each bounce suggest that all three adiabatic invariants are violated. Details characterizing this process are presented in Figure 2c–2h showing the temporal variation in L, first adiabatic invariant (μ_a) and energy (E_n) along with probability distributions (PDFs) describing

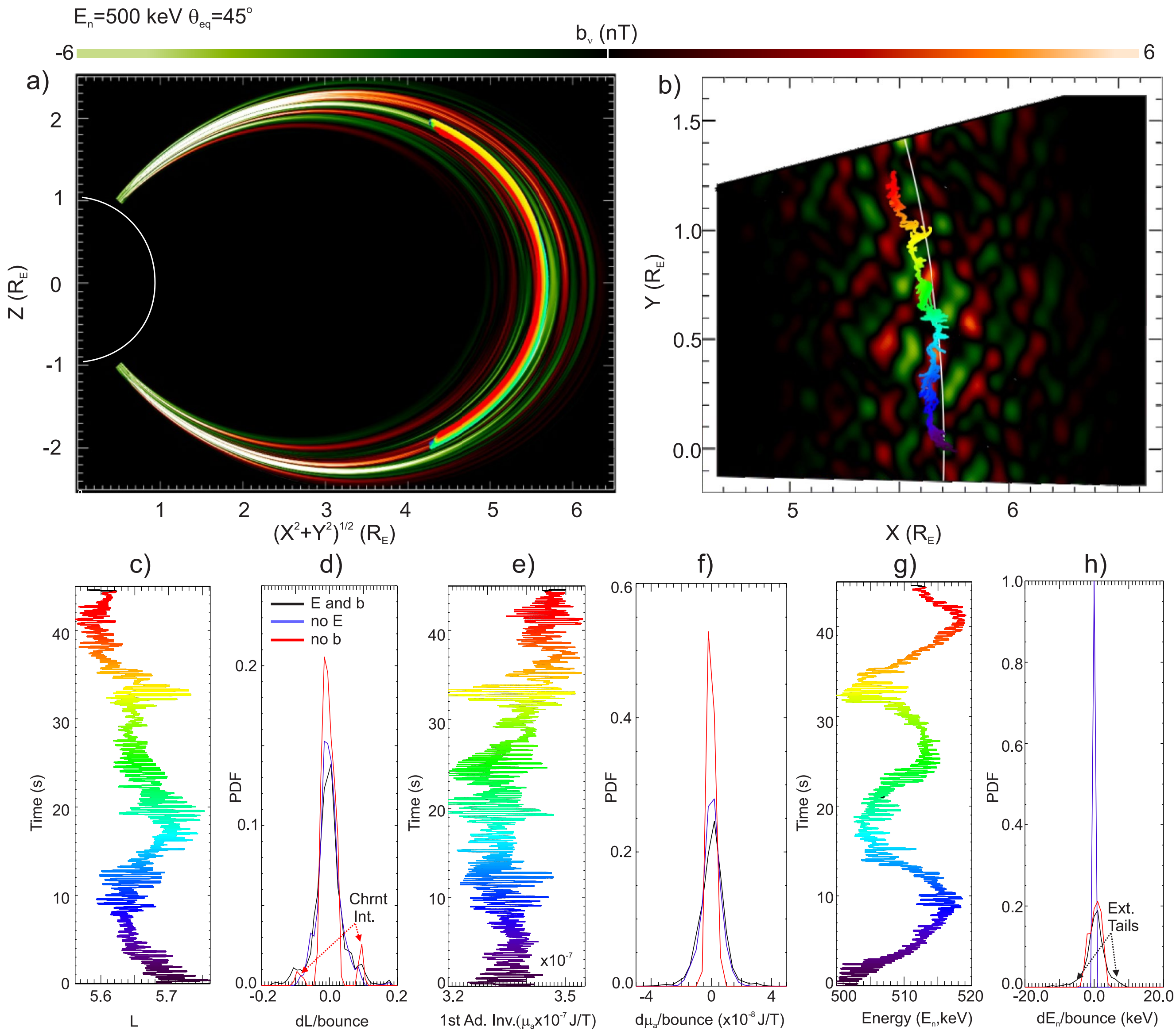

Figure 2. Electron transport at $E_n = 500$keV, $\theta_{eq} = 45^o$ and $L_0 = 5.7$. (a) Electron trajectory projected into the $\sqrt{X^2 + Y^2}$, Z plane superimposed on b_ν field model midflight. Rainbow color scale shows time. (b) Electron trajectory mapped adiabatically into the equatorial plane. (c–h) L-shell, first adiabatic invariant (μ_a) and energy (E_n) along the trajectory with corresponding bounce averaged PDFs.

the statistics of displacements in each quantity over a bounce. While it is difficult to identify the operation of specific wave-particle resonances within the broad-band spectrum, these displacements and the distributions they provide can be understood in terms of the integrated effect of the electromagnetic forces acting along the drift-bounce orbit of an electron in the dipolar geomagnetic field (Chaston et al., 2017; Chaston, Bonnell, Wygant, et al., 2018; Chaston, Bonnell, Halford, et al., 2018; Dungey, 1964). In the following gyro-average expressions describing the associated transport rates arising from these forces are provided with the derivation and a more complete description of each contribution given in the references cited.

The variations in L are predominately due to the distortion of the geomagnetic field associated with fluctuations in b (Chaston, Bonnell, Wygant, et al., 2018). This is demonstrated in Figure 2d showing the PDF of bounce-averaged displacements through L-shell with the perturbed magnetic field everywhere equal to zero (red curve), the rest frame electric field equal to zero (blue) and the full electromagnetic fields (black). Here the distribution accumulated in the full electromagnetic fields is nearly identical to that accumulated in the absence of E except in the tails of the distribution. For the prescribed values of E_n and θ_{eq}, $|\frac{v_\mu b_\nu}{B_0}| > |E_\phi/B_0|$ and the transport across L-shells along a bounce-drift orbit is dominated by effective $v_\mu b_\nu/B_0$ drifts with rate (Dungey, 1964, Equation 29),

$$\frac{dL}{dt} \approx v_\mu b_\nu L^3 \, sin^3 \, \lambda / B_0 R_E \tag{8}$$

where λ is the colatitude and R_E the Earth radius. The tails in the distribution apparent in the full electromagnetic field case (Figure 2d, black curve) are a consequence of an interval of extended coherent interaction with large-scale E_ϕ (Chaston et al., 2017). This effect is manifest as the secondary peaks bracketing the central distribution of Figure 2d that appear when b is absent (red curve).

The variation in μ_a in Figure 2e is also mostly a consequence of distortions of the geomagnetic field. This is demonstrated in Figure 2f which shows that the PDF is almost unaltered if E is set to zero (blue curve) but is substantially reduced in width if b is set to zero (red curve). Noting that $\omega/\Omega_e \ll 1$, the "observed" transport is a consequence of reversible changes in μ_a associated with radial transport in the distorted geomagnetic field on large scales and irreversible changes due to pitch-angle scattering off gyro-radii scale structuring in b (Chaston, Bonnell, Halford, et al., 2018). In a single mode the gyro-averaged rate of change in μ_a along an electron orbit via the scattering process is,

$$\frac{d\mu_a}{dt} \approx \Omega_e \cos^2\theta \frac{\nabla_\mu b_\perp}{k_\perp {B_0}^2} \left(\gamma^2 - 1\right) m_o c^2 [\cos(k_\perp \rho_e + \psi) - J_o(k_\perp \rho_e)\cos(\psi)] \tag{9}$$

(Chaston, Bonnell, Halford, et al., 2018; Equations 3 and 6)) where $b_\perp$ and $k_\perp$ are orthogonal and ψ is the location of the gyro-center with respective to wave phase. The displacements in μ_a that compose the distribution of Figure 2f are representative of the integration of Equation 9 over intervals of coherency with specific modes in the broad-band model.

On the other hand, the variations in E_n shown in Figure 2g are necessarily due to acceleration in E. Consequently, in Figure 2h the distribution of displacements in E_n when E is set to zero (blue curve) has values only in the $\Delta E_n = 0$ bin. Here E_ϕ accelerates/decelerates electrons along the drift orbit at rate,

$$\frac{dE_n}{dt} = q_e E_\phi v_d \tag{10}$$

where v_d is the azimuthal drift velocity. This is complemented by finite gyro-radii effects related to the pitch-angle scattering described above that provide,

$$\frac{dE_n}{dt} \approx \Omega_e \, cos \, \theta \frac{\nabla_\mu E_\perp}{k_\perp v B_0} m_o c^2 \left(\frac{\gamma^2 - 1}{\gamma}\right) [\cos(k_\perp \rho_e + \psi) - J_o(k_\perp \rho_e) cos(\psi)] \tag{11}$$

modified from Chaston, Bonnell, Halford, et al. (2018; Equations 2 and 6) for $E_\perp$. The electric field parallel to B_0 (E_μ) alters details of the trajectories but does not appreciably affect the PDFs for the energy considered. In contrast, finite b, while not contributing directly to acceleration, facilitates drifts across equipotentials leading to the enhanced energization. In Figure 2h this second order effect provides the extended width of the distribution in the full electromagnetic fields (black curve) relative to that compiled in the absence of b (red curve).

4. Transport Coefficients

The nearly Gaussian form of the PDFs for displacements in L, μ_a, and E_n along the trajectory shown in Figure 2 is suggestive of a "random-walk." Assuming for now that this description is appropriate, bounce averaged transport coefficients for stochastic transport in the turbulent fields can be estimated as,

$$D_{xx} = (\Delta x)^2 / 2 n_b \tau_b \tag{12}$$

where τ_b is the bounce period, n_b is the number of bounces over which the distribution is compiled and Δx is the standard deviation of the PDF. To derive estimates for those coefficients most relevant to radiation belt

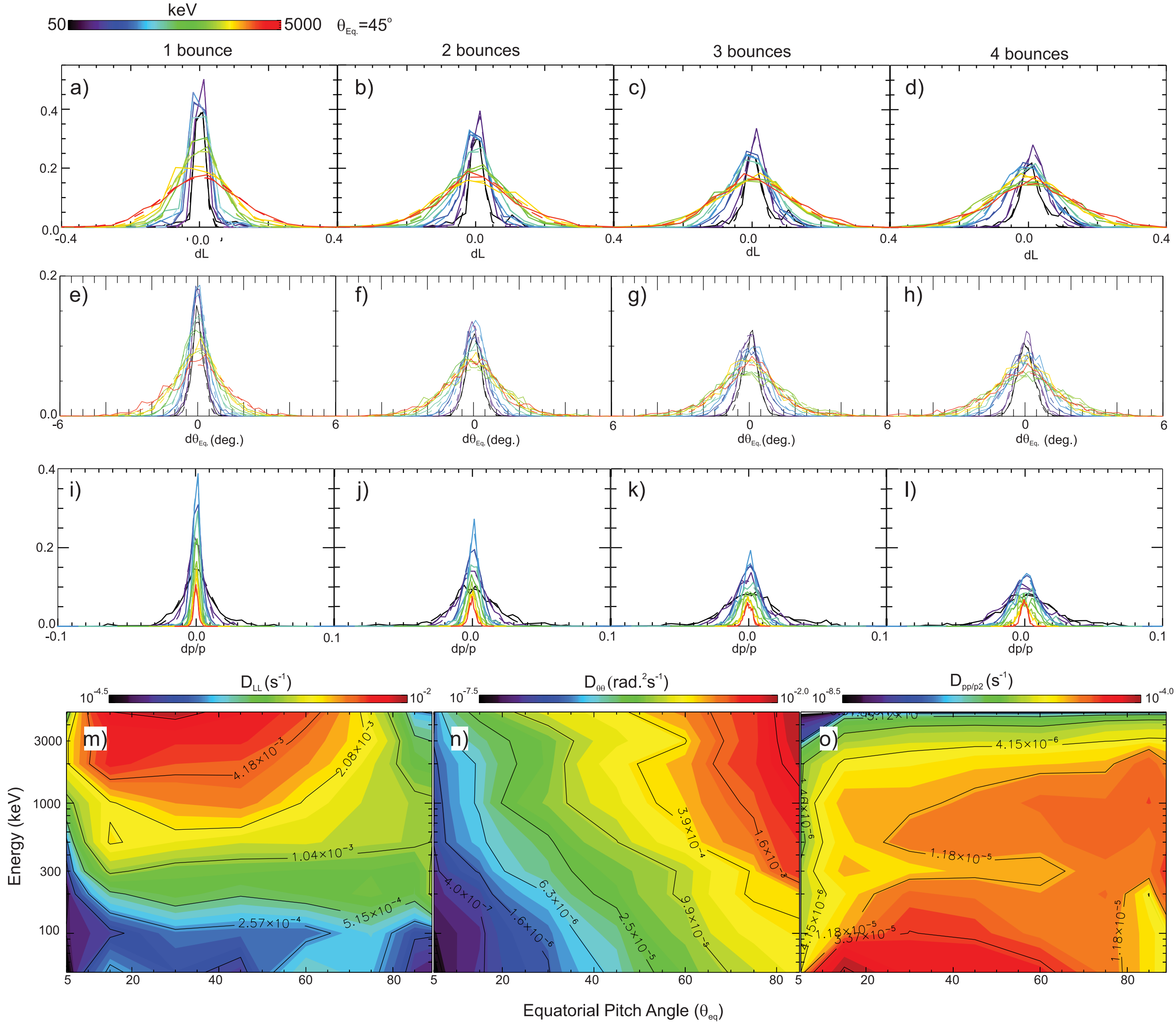

Figure 3. PDFs and transport coefficients at $\theta_{eq} = 45°$ and $L_0 = 5.7$. (a–d) PDFs in L averaged over $n_b = 1,2,3,4$ bounces. Colored lines show PDFs for energies $E_n = 50$, 100, 200, 300, 500, 1,000, 2,000, 3,000, 5,000 keV with the dashed lines being Gaussian fits. e-h) PDFs in θ_{eq}. (i–l) PDFs in p (normalized). m-o) Bounce averaged transport coefficients in L-shell, θ_{eq} and p (normalized).

transport, the distribution of displacements in L, θ_{eq}, and p over $n_b = 1, 2, 3, 4$ bounces at $L \approx 5.7$ from the simulation are compiled for a range of radiation belt energies and pitch-angles. Here $p = \gamma m_e v$ is the scalar momentum with $v = \sqrt{v_v{}^2 + v_\phi{}^2 + v_\mu{}^2}$. Results for $\theta_{eq} = 45°$ are presented in Figure 3 with the colored lines in Figure 3a–3l showing PDFs for energies, $E_n = 50$, 100, 200, 300, 500, 1,000, 2,000, 3,000, 5,000 keV and the dashed curves showing Gaussian fits to each PDF. Moving from left to right the progressive increase in the width of the distribution in each panel with the number of bounces considered is qualitatively consistent with a diffusive process.

Figure 3m–3o show the bounce-average transport coefficients derived via the process described above for the same energies extended to equatorial pitch-angles, $\theta_{eq} = 5°$, 15°, 30^o, 45°, 60°, 75°,85°, 89°. These coefficients are averages of those evaluated at $n_b = 1, 2, 3, 4$. The transport characterized by these coefficients is the consequence of interactions over the full range of wave temporal and spatial scales comprising the model spectrum with a morphology in E_n–θ_{eq} space that can be understood in terms of those transport mechanisms described above.

The coefficients for transport across L-shells, (D_{LL}), in Figure 3m increase with increasing energy and, except for the most field-aligned electrons, decrease with increasing pitch-angle. This morphology arises because increases in energy with decreasing pitch-angle necessarily increase v_μ and so from Equation 8 increase $\frac{dL}{dt}$. For the most field-aligned electrons however, the increased average strength of B_0 over a bounce counteracts the effect of increasing v_μ and leads to reduced transport. The resulting morphology shown in Figure 3m is equivalent to that provided from quasi-linear calculations (Chaston, Bonnell, Wygant, et al., 2018; Figures 3i and 3j) for drift bounce resonances in the same wave spectrum. Notably, the corresponding diffusive timescales ($1/D$) are less than a drift period.

The coefficients for transport in θ_{eq}, ($D_{\theta\theta}$), shown in Figure 3n increase with pitch-angle and energy. This is a consequence of increasing gyro-radius with both energy and pitch-angle in the inverse power-law spectrum of fluctuations in b shown in Figure 1c. Expressing Equation 9 in terms of θ, the gyro-averaged rate of change in pitch-angle along an electron orbit in a single wave is,

$$\frac{d\,sin(\theta/2)}{dt} \approx \frac{\Omega_e}{2} cot\,\theta \frac{\nabla_\mu b_\perp}{k_\perp B_0}[\cos(k_\perp \rho_e + \psi) - J_o(k_\perp \rho_e) cos(\psi)] \tag{13}$$

(Chaston, Bonnell, Halford, et al., 2018; Equation 7). The inverse power-law k-spectrum provides larger $b_\perp$ at larger scales, so as the gyro-radius increases the average change in wavefield amplitude across the orbit increases leading to enhanced scattering - hence the increase in $D_{\theta\theta}$ with E_n and θ_{eq}. The larger amplitudes encountered by field-aligned electrons that mirror at high-latitudes do not provide increases in $D_{\theta\theta}$ for small θ_{eq} because the $k_\perp \rho_e \propto [\theta, 1/B_0]$ dependency through Equation 13 acts to reduce bounce averaged $\frac{d\,sin(\theta/2)}{dt}$. A similar morphology is returned via quasi-linear calculations for the same process based on the action of b_ν alone (Chaston, Bonnell, Halford, et al., 2018; Figure 3i–3k). Notably, the combined action of b_ν and of b_ϕ represented in Figure 3n enhances the magnitudes of these coefficients from the quasi-linear estimate to provide scattering of MeV electrons at large θ_{eq} on diffusive timescales as short as 100 s.

The action of the electric fields allow the transfer of wave energy and transport in scalar momentum space represented in Figure 3o as D_{pp/p^2}. These coefficients are a consequence of the same processes that drive radial transport and pitch-angle scattering quantified in Figures 3m and 3n albeit without the same energy dependency. Specifically, the dependency on $1/v$ in Equation 11 counteracts the tendency for D_{pp/p^2} to increase with gyro-radius so that unlike $D_{\theta\theta}$, D_{pp/p^2} does not generally increase with E_n. Quasi-linear estimates (Chaston et al., 2017, Figures 3i and 3j) indicate the action of E_ϕ is most important at low energies and small pitch-angle with a morphology in E_n–θ_{eq} space like that shown in Figure 3o. The action of the full spectrum of field variations shown here provides bounce-averaged transport coefficients in momentum space comparable to that expected in whistler mode chorus (Summers et al., 2007) with particular efficacy for $E_n \lesssim 100$ keV.

5. Discussion and Conclusion

The transport coefficients derived in this study represent the integrated effect of all the field components in the empirically derived wave model along each electron orbit. The dominant contributions to the transport across L-shells arise through the action of b_ν, while the combined action of b_ν and b_ϕ drive transport through pitch-angle. The transport through momentum space is a consequence of the equivalent processes in E_ϕ, that also contributes to transport across L-shells, and the action of electron gyro-radius scale variations in E_ν and E_ϕ that together drive perpendicular energization. While it is difficult to identify the operation of specific resonances along electron orbits in the broad-band spectrum, these results largely confirm quasi-linear estimates for drift-bounce resonances (Chaston et al., 2017; Chaston, Bonnell, Wygant, et al., 2018; Chaston, Bonnell, Halford, et al., 2018) albeit returning somewhat larger values. This enhancement is due to the simultaneous action of all field components that allows second order contributions and the superposition of contributions from multiple modes and bounce harmonics.

The simulation allows an evaluation of the applicability of a diffusive model to the "observed" transport. Intervals of extended coherent interaction for example, violate the "random-walk" ansatz and generate extended tails in the PDFs and non-linearity in the temporal evolution of $(\Delta x)^2$. Figure 4 shows the evolution of $(\Delta x)^2$, in L-shell, θ_{eq} and p at representative electron energies and pitch-angles derived by compiling the PDF of displacements in each transport quantity over intervals defined by n_b as labeled on the abscissae. As earlier, this is performed

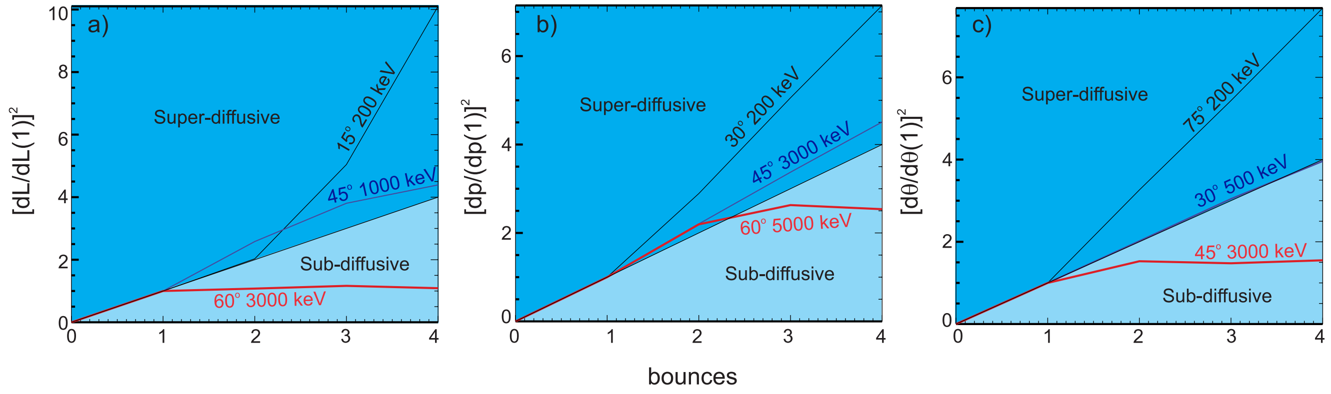

Figure 4. Transport coefficient variation with $n_b = 1, 2, 3, 4$ for representative E_n and θ_{eq} values. Classical diffusion occurs along the interface between light and dark blue regions.

by tracing the trajectory of a single electron at each E_n- θ_{eq} over many bounces. Note that ΔL, $\Delta\theta_{eq}$, and Δp are small relative to L, θ_{eq}, and p and the PDFs are symmetric. For classical diffusion (CD) the curves at each E_n and θ_{eq} in Figure 4 should follow a straight line such that $(\Delta x)^2/2n_b\tau_b$ is constant and $(\Delta x)^2 \propto t^\gamma$ with $\gamma = 1$. If $\gamma \neq 1$ then the temporal evolution of $(\Delta x)^2$ is "non-linear." CD is represented in Figure 4 by the line dividing the light and dark blue regions. Above this line the transport is described as super-diffusive ($\gamma > 1$; faster than CD) and below this line is termed sub-diffusive ($\gamma < 1$; slower than CD) (Zimbardo et al., 2015). All three categories of diffusion can be found in the PDFs compiled from the particle simulations, with a transition from super-diffusive to sub-diffusive behavior with increasing energy and pitch-angle—or more specifically increasing gyro-radius. This dependency is analogous to observations in laboratory experiments (Bovet et al., 2015) of supra-thermal ion transport in interchange turbulence. Further analysis is required to assess the impact of sub/super diffusion on radiation belt transport.

Finally, it is emphasized that these simulations are performed without assumptions concerning the nature of the wave-particle interaction. The bounce averaged transport coefficients consequently represent the effect of the full spectrum of broadband fluctuations on outer radiation belt electrons irrespective of the underlying mechanisms. Notably, this numerical experiment returns coefficients comparable to, or larger than the equivalent coefficients in those wave modes classically identified to drive outer radiation belt transport including whistler mode chorus, electromagnetic ion cyclotron waves (Summers et al., 2007) and MHD ULF waves (Li et al., 2016). Given the prevalence of Alfvénic turbulence during geomagnetic storms it may be expected that these fluctuations play a role in the storm-time evolution of the outer radiation belt.

Data Availability Statement

The eigenmode solutions and plasma model defining the turbulent wavefields, along with files containing the transport quantities extracted from the particle tracing that provide the results described in this manuscript are available at https://figshare.com/articles/dataset/Data_files_for_submission_Electron_Scattering_Transport_and_Energization_by_Alfv_nic_Turbulence_in_Earth_s_Outer_Radiation_Belt_by_C_C_Chaston_to_Geophysical_Research_Letters/22672933. A PDF file describing the file contents and format is also provided at this site.

Acknowledgments
The author thanks the Van Allen Probes team for the in-situ measurements which motivated this study and defined the field model. This research was supported by NSF Grant 2041971 and NASA Grant NNX17AI55G.

References

Baker, D. N., Jaynes, A. N., Kanekal, S. G., Foster, J. C., Erickson, P. J., Fennell, J. F., et al. (2016). Highly relativistic radiation belt electron acceleration, transport, and loss: Large solar storm events of March and June 2015. *Journal of Geophysical Research: Space Physics*, *121*(7), 6647–6660. https://doi.org/10.1002/2016JA022502

Bale, S. D., Kellogg, P. J., Mozer, F. S., Horbury, T. S., & Reme, H. (2005). Measurement of the electric fluctuation spectrum of magnetohydrodynamic turbulence. *Physical Review Letters*, *94*(21), 215002. https://doi.org/10.1103/physrevlett.94.215002

Bovet, A., Fasoli, A., Ricci, P., Furno, I., & Gustafson, K. (2015). Nondiffusive transport regimes for suprathermal ions in turbulent plasmas. *Physical Review E*, *91*(4), 041101. https://doi.org/10.1103/PhysRevE.91.041101

Chaston, C. C. (2022). Flow channels and the generation of Alfvénic turbulence along storm-time inner magnetospheric field-lines. *Geophysical Research Letters*, *49*(23), e2022GL101321. https://doi.org/10.1029/2022GL101321

Chaston, C. C., Bonnell, J. W., Halford, A. J., Reeves, G. D., Baker, D. N., Kletzing, C. A., & Wygant, J. R. (2018). Pitch angle scattering and loss of radiation belt electrons in broadband electromagnetic waves. *Geophysical Research Letters*, *45*(18), 9344–9352. https://doi.org/10.1029/2018gl079527

Chaston, C. C., Bonnell, J. W., Kletzing, C. A., Hospodarsky, G. B., Wygant, J. R., & Smith, C. W. (2015). Broadband low-frequency electromagnetic waves in the inner magnetosphere. *Journal of Geophysical Research: Space Physics*, *120*(10), 8603–8615. https://doi.org/10.1002/2015JA021690

Chaston, C. C., Bonnell, J. W., Reeves, G. D., & Skoug, R. M. (2016). Driving ionospheric outflows and magnetospheric O^+ energy density with Alfvén waves. *Geophysical Research Letters*, *43*(10), 4825–4833. https://doi.org/10.1002/2016GL069008

Chaston, C. C., Bonnell, J. W., Wygant, J. R., Mozer, F., Bale, S. D., Kersten, K., et al. (2014). Observations of kinetic scale field line resonances. *Geophysical Research Letters*, *41*(2), 209–215. https://doi.org/10.1002/2013GL058507

Chaston, C. C., Bonnell, J. W., Wygant, J. R., Reeves, G. D., & Baker, D. N. (2020). Filamentary currents and Alfvénic vortices in the inner magnetosphere. *Geophysical Research Letters*, *47*(4), e2019GL086318. https://doi.org/10.1029/2019GL086318

Chaston, C. C., Bonnell, J. W., Wygant, J. R., Reeves, G. D., Baker, D. N., & Melrose, D. B. (2018). Radiation belt “dropouts” and drift-bounce resonances in broadband electromagnetic waves. *Geophysical Research Letters*, *45*(5), 2128–2137. https://doi.org/10.1002/2017GL076362

Chaston, C. C., Bonnell, J. W., Wygant, J. R., Reeves, G. D., Baker, D. N., Melrose, D. B., & Cairns, I. H. (2017). Radial transport of radiation belt electrons in kinetic field-line resonances. *Geophysical Research Letters*, *44*(16), 8140–8148. https://doi.org/10.1002/2017GL074587

Cummings, W. D., O'Sullivan, R. J., & Coleman, P. J., Jr. (1969). Standing Alfvén waves in the magnetosphere. *Journal of Geophysical Research*, *74*(3), 778–793. https://doi.org/10.1029/JA074i003p00778

Dungey, J. (1964). Effects of electromagnetic perturbations on particles trapped in the radiation belts. *Space Science Reviews*, *4*(2), 199–222. https://doi.org/10.1007/bf00173882

Horne, R. B., & Thorne, R. M. (1998). Potential waves for relativistic electron scattering and stochastic acceleration during magnetic storms. *Geophysical Research Letters*, *25*(15), 3011–3014. https://doi.org/10.1029/98gl01002

Hull, A. J., Chaston, C. C., Bonnell, J. W., Damiano, P. A., Wygant, J. R., & Reeves, G. D. (2020). Correlations between dispersive Alfvén wave activity, electron energization, and ion outflow in the inner magnetosphere. *Geophysical Research Letters*, *47*(17), e2020GL088985. https://doi.org/10.1029/2020GL088985

Johnson, J. R., & Cheng, C. Z. (1997). Kinetic Alfvén waves and plasma transport at magnetopause. *Geophysical Research Letters*, *24*(11), 1423–1426. https://doi.org/10.1029/97gl01333

Li, Z., Hudson, M., Paral, J., Wiltberger, M., & Turner, D. (2016). Global ULF wave analysis of radial diffusion coefficients using a global MHD model for the 17 March 2015 storm. *Journal of Geophysical Research: Space Physics*, *121*(7), 6196–6206. https://doi.org/10.1002/2016JA022508

Mann, I. R., Wright, A. N., & Cally, P. S. (1995). Coupling of magnetospheric cavity modes to field line resonances: A study of resonance widths. *Journal of Geophysical Research*, *100*(A10), 19441–19456. https://doi.org/10.1029/95JA00820

Mauk, B. H., Fox, N. J., Kanekal, S. G., Kessel, R. L., Sibeck, D. G., & Ukhorskiy, A. (2012). Science objectives and rationale for the radiation belt storm probes mission. https://doi.org/10.1007/s11214-012-9908-y

Millan, R. M., & Thorne, R. M. (2007). Review of radiation belt relativistic electron losses. *Journal of Atmospheric and Solar-Terrestrial Physics*, *69*(3), 362–377. https://doi.org/10.1016/j.jastp.2006.06.019

Ozeke, L. G., Mann, I. R., Murphy, K. R., Sibeck, D. G., & Baker, D. N. (2017). Ultra-relativistic radiation belt extinction and ULF wave radial diffusion: Modeling the September 2014 extended dropout event. *Geophysical Research Letters*, *44*(6), 2624–2633. https://doi.org/10.1002/2017GL072811

Rae, I. J., Murphy, K. R., Watt, C. E. J., Sandhu, J. K., Georgiou, M., Degeling, A. W., et al. (2019). How do ultra-low frequency waves access the inner magnetosphere during geomagnetic storms? *Geophysical Research Letters*, *46*(19), 10699–10709. https://doi.org/10.1029/2019GL082395

Shen, Y., Artemyev, A., Zhang, X.-J., Angelopoulos, V., An, X., & Runov, A. (2022a). Energetic electron scattering by kinetic Alfvén waves at strong magnetic field gradients of dipolarization front. *Physics of Plasmas*, *29*(8), 082901. https://doi.org/10.1063/5.0096338.(.

Shen, Y., Artemyev, A. V., Zhang, X.-J., Angelopoulos, V., Vasko, I., Turner, D., et al. (2022b). Tens to hundreds of keV electron precipitation driven by kinetic Alfvén waves during an electron injection. *Journal of Geophysical Research: Space Physics*, *127*(8), e2022JA030360. https://doi.org/10.1029/2022JA030360

Summers, D., Ni, B., & Meredith, N. P. (2007). Timescales for radiation belt electron acceleration and loss due to resonant wave-particle interactions: 2. Evaluation for VLF chorus, ELF hiss, and electromagnetic ion cyclotron waves. *Journal of Geophysical Research*, *112*(A4), A04207. https://doi.org/10.1029/2006JA011993

Turner, D. L., Shprits, Y., Hartinger, M., & Angelopoulos, V. (2012). Explaining sudden losses of outer radiation belt electrons during geomagnetic storms electrons during geomagnetic storms. *Nature Physics*, *8*(3), 208–212. https://doi.org/10.1038/nphys2185

Usanova, M. E., & Ergun, R. E. (2022). Electron energization by high-amplitude turbulent electric fields: A possible source of the outer radiation belt. *Journal of Geophysical Research: Space Physics*, *127*(7), e2022JA030336. https://doi.org/10.1029/2022JA030336

Zimbardo, G., Amato, E., Bovet, A., Effenberger, F., Fasoli, A., Fichtner, H., et al. (2015). Superdiffusive transport in laboratory and astrophysical plasmas. *Journal of Plasma Physics*, *81*(6), 495810601. https://doi.org/10.1017/S0022377815001117